2021 43rd Annual International Conference of the
IEEE Engineering in Medicine & Biology Society (EMBC)
Oct 31 - Nov 4, 2021. Virtual Conference

Adaptable Class-D Power Amplifier based Power Modulation and Data Transfer Technique for Biomedical Systems

Sayan Sarkar, Student *Member, IEEE*

***Abstract*— Class-D half and full-bridge power amplifiers (PA) finds their usefulness in wireless power transfer (WPT) blocks for a biomedical implant. This brief presents a 13.56-MHz wireless power transfer system using an adaptive PA structure and digital control scheme for providing sufficient power during downlink data transfer. This scheme prevents efficiency degradation due to amplitude modulation. Simultaneously changing PA structure and operating frequency gives a higher degree of freedom for power modulation. The transmitter and receiver sides were designed in the 0.18-µm CMOS process using 1.8 V and 5 V devices.**

***Keywords* — Coupled coil, Full-bridge, Half-bridge, Demodulator, Implant**

I. Introduction

In recent days, WPT technologies are gaining much attention for powering implantable medical devices or implants, such as neural, cochlear, and retinal implants [1]. Typically, a Class-D PA is used to drive the primary side of a WPT by switching on and off systematically using rectangular waves. Let us assume the primary tank's resonant frequency to be f_o. Different switching mechanisms are used for power control. They are - (1) Sub-harmonic frequency control, [1] f_{sw} is changed among odd sub-harmonics f_o, $f_o/3$, $f_o/5$ (2) Continuous frequency modulation control: (f_{sw} is varied continuously in the resonance frequency neighborhood at high coupling conditions under split frequency effect) [2]. In prior undertakings, researchers had developed the inductor current modeling for half-bridge PA [3]. Recent trends show that circuit designers prefer to shift from half-bridge [4] to full-bridge PA design [4] for higher power transfer. Naturally, the input voltage $V_s(t)$ to the circuit is also changed [5]-[9]. This research has used primary inductor current as a benchmarking tool for such bio-medical systems for power transfer purposes.

II. Modeling of Coil System

Coupled coils structure with a series resonant primary and parallel resonant secondary sides follows Fig. 1. The couple coils equations using KVL for both the primary and secondary sides are given by (1) & (2).

$$V_I(t) = L_1\frac{dI_1(t)}{dt} - M\frac{dI_2(t)}{dt} \quad (1)$$

$$V_{II}(t) = M\frac{dI_1(t)}{dt} - L_2\frac{dI_2(t)}{dt} \quad (2)$$

Sayan Sarkar was with Wecare Medservice LLP.
He is now with Hong Kong University of Science and Technology
sayansarkarust@gmail.com

The mutual inductance is M, resonance frequency is given as $f_o = \omega_o/2\pi$. Coupling coefficient k and turns-ratio n are

$$\omega_o = \frac{1}{\sqrt{L_1C_1}} = \frac{1}{\sqrt{L_2C_2}} \quad (3)$$

$$k = \frac{M}{\sqrt{L_1L_2}}, \qquad n = \sqrt{\frac{L_2}{L_1}} \quad (4)$$

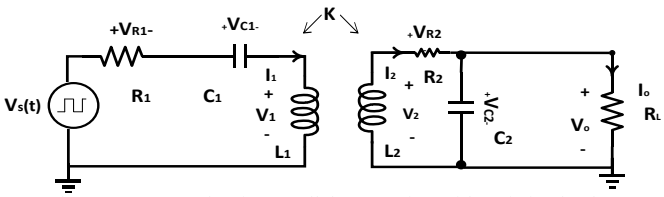

Fig. 1. Structure of series-parallel connection with resistive load

For the coupling less ($k = 0$) primary section, we have (5)[4].

$$V_s(t) = I_1(t)R_1 + \frac{1}{C_1}\int^t I_1(\tau)d\tau + L_1\frac{dI_1(t)}{dt} \quad (5)$$

The input voltage to the circuit is $V_{s.}(s)$, and the subsequent Laplace transform of (5) gives (6) [4].

$$I_1(s) = \frac{V_s(s)}{L_1}\frac{s}{\left(s^2 + 2\zeta_1\omega_o s + \omega_o^2\right)} \quad (6)$$

Where the damping factor ζ_1 and the quality factor Q_1 are

$$2\zeta_1\omega_o = \frac{R_1}{L_1}, \qquad Q_1 = \frac{1}{2\zeta_1} = \frac{\omega_o L_1}{R_1} = \frac{1}{R_1}\sqrt{\frac{L_1}{C_1}} \quad (7)$$

Current in (6) is valid without any secondary side. Inductor current in time-domain for half-bridge Class- D PA follows (8) [4].

$$I_1(t) = \frac{V_A}{R_1}\frac{2\zeta_1}{\left(1-\zeta_1^2\right)^{1/2}}\frac{e^{-\zeta_1\omega_o t}}{\left(1-e^{-\zeta_1\pi}\right)}\sin\left(1-\zeta_1^2\right)^{1/2}\omega_o t \quad (8)$$

A. Switching at the resonant frequency

For a Full-bridge Class-D PA, the MOS power switches are switched on and off periodically with time period T. At $f_{sw}=f_o=1/T$, and the primary coil is driven by a rectangular wave $V_{s.}(t)$ that switches between V_A and $-V_A$:

$$\begin{pmatrix} V_s(t) = V_A & 0 \le t < T/2 \\ V_s(t) = -V_A & T/2 \le t < T \end{pmatrix} \quad (9)$$

The periodic waveform of voltage in the time-domain and in the Laplace domain follows (10) and (11) [4].

$$V_s(t) = V_A\Sigma_{n=0}^{\infty}(u(t-nT) - 2u(t-(n+1/2)T + u(t-(n+1)T) \quad (10)$$

$$V_s(s) = \frac{V_A}{s}\Sigma_{n=0}^{\infty}\left(e^{-snT} - 2e^{-s\left(n+\frac{1}{2}\right)T} + e^{-s(n+1)T}\right) \quad (11)$$

Provided, u(t) denotes the Heaviside function. Summing (11) and substituting into (6) gives (12).

$$I_1(s) = \frac{V_A}{R_1}\left(\frac{1-e^{-sT/2}}{1+e^{-sT/2}}\right)\frac{2\zeta_1\omega_o}{\left(s^2+2\zeta_1\omega_o s+\omega_o^2\right)} \quad (12)$$

The exponential term ($1+e^{-sT/2}$) in the denominator of (12) reflects the anti-symmetric property of the function as per (13) [3]. Let $F_1(t)$ is a function with period 'T.'

$$F_1(t-T/2) = -F_1(t) \quad (13)$$

Note that

$$\frac{F_1(s)}{(1+e^{-sT/2})} = \Sigma_{n=0}^{\infty}(-1)^n e^{-snT/2}F_1(s) \quad (14)$$

Therefore, the inverse Laplace transform of (14) is

$$\mathcal{L}^{-1}\left\{\frac{F_1(s)}{1+e^{-sT/2}}\right\} = \Sigma_{n=0}^{\infty}(-1)^n F_1\left(t-\frac{nT}{2}\right)u\left(t-\frac{nT}{2}\right) \quad (15)$$

The transient inductor current in the time-domain is (16) where $t_n = t - \frac{nT}{2}$.

$$I_1(t) = \frac{V_A}{R_1}\frac{2\zeta_1}{\sqrt{1-\zeta_1^2}}\Sigma_{n=0}^{\infty}(-1)^n[sin\omega_o' t_n e^{-\zeta_1\omega_o t_n}u(t_n) - sin\omega_o'(t_n+\frac{T}{2})e^{-\zeta_1\omega_o\left(t_n+\frac{T}{2}\right)}u(t_n+\frac{T}{2})] \quad (16)$$

The steady-state current in the time-domain follows (17) upon summing all the terms in (16).

$$I_1(t) = \frac{V_A}{R_1}\frac{2\zeta_1}{\left(1-\zeta_1^2\right)^{\frac{1}{2}}}\frac{2e^{-\zeta_1\omega_o t}}{(1-e^{-\zeta_1\pi})}\sin\omega_o' t \quad (17)$$

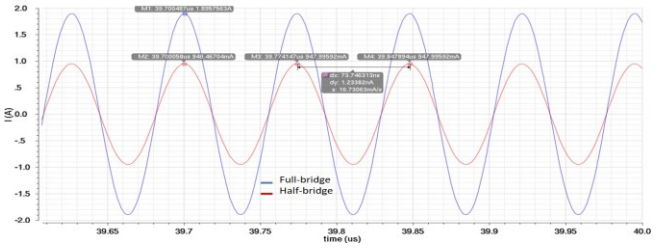

Fig. 2. Comparative analysis of half and full-bridge PA steady-state at f_o

TABLE I. INDUCTOR CURRENT SIMULATION PARAMETERS

Supply voltage V_A	1.0 V
Resonance frequency f_o	13.56 MHz
Primary coil inductance L_1	722 nH
Primary coil capacitance C_1	190.18 pF
Primary coil parasitic resistance R_1	0.36 Ω
PA turn on resistance	0.24 Ω
Secondary coil inductance L_2	458 nH
Secondary coil capacitance C_2	300.78 pF
Secondary coil parasitic resistance R_2	1.617 Ω
Load Resistance R_L	4 kΩ
Coupling coefficient (k_{12})	1.5% (~20 mm)

We simulated the full-bridge system as per Table I, and the inductor current is reported in Fig. 2. It is well acknowledged from simulation and calculation results that the full-bridge PA's inductor current is 2 times larger [4] than the half-bridge PA's inductor current. The simulated and calculated inductor current are available in Table II based on ANSYS HFSS derived coil parameters in Table I. The calculated and simulated currents are accurate up to 92%.

TABLE II. SIMULATED & CALCULATED VALUES COMPARISON

Type of PA	Simulated amplitude	Calculated amplitude
Half-bridge PA	0.947A	1.05A
Full-bridge PA	1.895A	2.1A

The overall emitted power is 4 times larger in full-bridge PA than half-bridge PA. This variation of the inductor current can be used for power modulation and power embedded data modulation [4]. During sub-harmonic frequency operation ($f_o/3$), the inductor current is divided by three as per (18) and (19) depending on full-bridge or half-bridge operating condition. The modulation depth (MD) of the ASK (amplitude shift keying) signal often has to be 8%–100% to achieve decent sensitivity in the WPT receiver. It deteriorates the power conversion efficiency (PCE) of the WPT receiver as per (20), where 'E' stands for effective, and 'PCE' stands for power conversion efficiency [7].

$$I_1(t) = \frac{V_A}{R_1}\frac{2\zeta_1}{\left(1-\zeta_1^2\right)^{\frac{1}{2}}}\frac{e^{-\zeta_1\omega_o t}}{(1-e^{-3\zeta_1\pi})}\sin\omega_o' t \quad (18)$$

$$I_1(t) = \frac{V_A}{R_1}\frac{2\zeta_1}{\left(1-\zeta_1^2\right)^{\frac{1}{2}}}\frac{2e^{-\zeta_1\omega_o t}}{(1-e^{-3\zeta_1\pi})}\sin\omega_o' t \quad (19)$$

$$EPCE = \frac{1+MD^2}{(1+MD)^2}PCE \quad (20)$$

III. Discussion on the Secondary Side of the System

The typical architecture of the secondary side of a wireless implant follows Fig. 3(a). The secondary side is operating under wireless series-parallel architecture. Front and back end protection circuits are used for the protection of the implant side. The 'Backscattering unit' is used for uplink data transmission based on 'load-shift keying.' However, detailed discussion of front end and back end protection, BGR, LDOs (useful for additional features) are omitted in this discussion. The focus is directed on power modulation and data transfer-related discussion. The downlink data is ASK modulated, and an envelope detector is used as the implant demodulator, as shown in Fig. 3(b). The demodulator has a peak detector, a band-pass (BP) filter, and a Schmitt trigger comparator. The peak detector filters out most of the resonance frequency components, and BP filters out noise and captures the clean data. Data is sent to the Schmitt trigger comparator for quantization. In the steady-state, V_m is a DC voltage of $V_o/2$ and is connected to the negative input terminal in- of the Schmitt trigger comparator. These data signals are single-ended that drives the positive input terminal in+ [6]. The Schmitt trigger comparator has two negative thresholds: −0.12 V and −0.2 V. In the idle state, in+ is almost equal to in-, and the output is "High." When "1" is transmitted, it is the same as the idle state. When "0" is transmitted, if the negative pulse goes

below −0.2 V, the output will be triggered to "Low." Negative pulses due to noise or power regulation with amplitudes lower than 0.2 V are rejected. When it is going above -0.12 V, the system's initial state is restored [6].

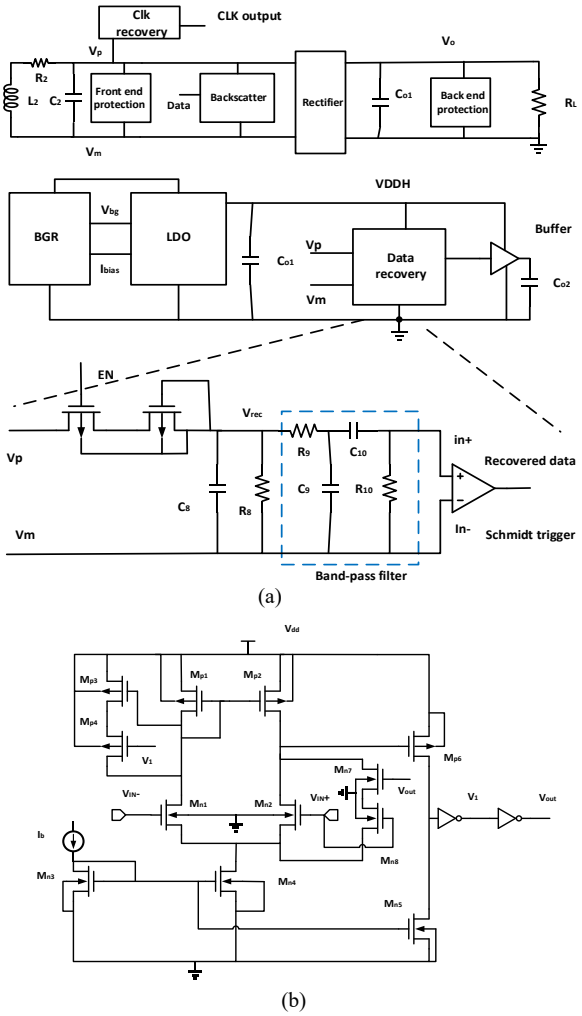

Fig. 3. (a)Typical architecture of secondary side of a wireless implant architecture, (b) Schmidt trigger circuit

The Schmitt trigger comparator follows Fig. 3(b). The input transistor pair and the current mirror circuit are designed not to be matched to generate different input offset voltages that serve as the negative threshold voltages. When the output is "low," MN_4 and MP_4 are turned off.

The mismatch between MN_1 and MN_2 and the mismatch between MP_1 and MP_2 together results in a negative triggering threshold of around −0.12 V. When the output is "high," MN_4 and MP_4 are turned on. The mismatch between MN_1 and (MN_2 + MN_3) and the mismatch between MP_2 and (MP_1 + MP_3) result in another negative triggering threshold of around −0.2 V [6]. We monitored the V_{out} signal in Fig. 3(b) during data demodulation for decoding the data.

IV. NEED OF CLASS- D PA ADAPTIVE STRUCTURE

In Class-D PA-based WPT, downlink data transmission is typically achieved by on-off keying (OOK) [8] or by switching frequency modulation schemes [1]. However, these techniques introduce problems in implant operation. Sudden reduction of current can shut down critical blocks of the implant. Abrupt power reduction is typically avoided by sending a bitstream [6] (example 1=1111, 0=1011) of high and low power. So, in worst-case conditions, the system receives at least 75% of the power. This bitstream keeps the sufficient power level by averaging method but reduces the effective data transmission speed. For a high downlink data rate, it is crucial to have a small bit width.

It is not always suitable for advanced neural implants [9] to stop the system (in the presence of a critical block) due to the unavailability of power. Suppose, if the system is toggling in between resonance and sub-harmonic frequency ($f_o/3$) for modulation, the current and power variation is nearly three and nine times. Similarly, if the system is toggling in between half-bridge and full-bridge PA, the current and power variations are nearly two and four times. Different mid-power levels are created in earlier literature by time-averaging [1]. In order to obtain even sub-harmonic frequency points like *fo*/4, odd sub-harmonic frequencies like *fo*/3 and *fo*/5 are alternately used. This averaging technique unnecessarily wastes some cycles for mid-power creation and reduces the data transfer rate. An adaptable PA structure is developed for intermediate power level development by simultaneously varying input voltage to the LC tank and switching frequency. For example, if the full-bridge PA is operated at a sub-harmonic frequency like ($f_{sw} = f_o/3, f_o/5$) case, the power variations are 2.25 times and 6.25 times respectively. This technique is helpful for downlink data transmission as well as prevents shut down of the overall system.

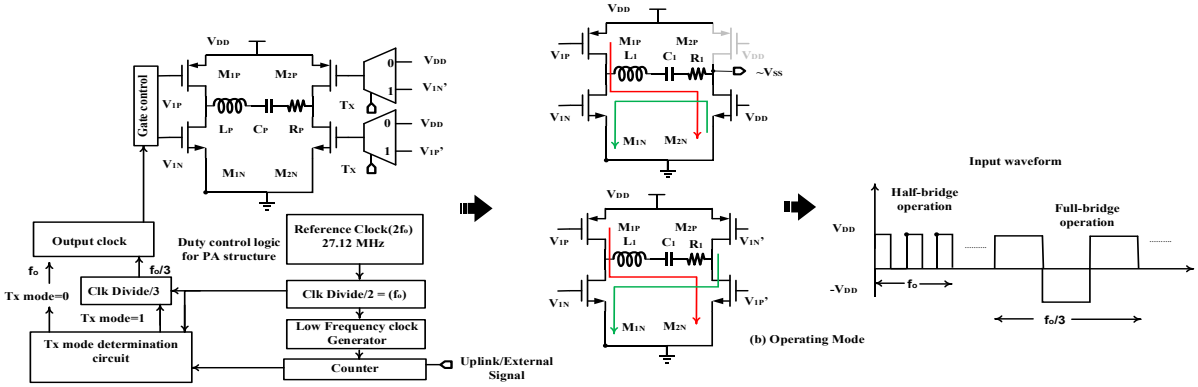

Fig. 4(a) Adaptive PA architecture, (b) Half-bridge and full-bridge operating mode with output waveform

V. ADAPTABLE CLASS- D PA OPERATION

Typically the system is operating in half-bridge class–D PA mode. The PA is switched to full bridge mode during power modulation or downlink data transfer, but the operating frequency changes to sub-harmonic frequency $(f_o/3)$ from the resonance frequency (f_o). The adaptive PA structure in Fig. 4(a) works as follows. The reference CLK is 27.12 MHz. The reference clock is 'divided by two' using a 'CLK divider' and supplied to the counter, Tx mode detector, second stage 'CLK divider' for low-frequency CLK generation. In steady-state conditions, power or data modulation is based on the uplink signal high condition during closed-loop operation or external input high condition during open-loop conditions. The counter starts counting for 25 cycles and updates the status of the Tx mode circuit. In Tx mode =1, the operating CLK is passed through a divider block and further divided by 3. As a result, the operating frequency is changed to $(f_o/3)$. The PA is switched to the full-bridge operating mode. The power level is reduced, as stated in the previous paragraph. Now the system is operating at a reduced current level for 35 cycles. Due to the complex structure of equivalent impedance between the primary and secondary sides, power reduction is not exactly three times. It is nearly 2 times, as observed from the secondary side induced voltage curve in Fig. 5. Thereafter, the uplink changes state (low), Tx mode = 0, the counter starts counting for 20 cycles. Operating frequency changes to resonance frequency (f_o) from sub-harmonic frequency$(f_o/3)$. In this way, single-bit data transmission is complete. The data is recovered in the secondary site.

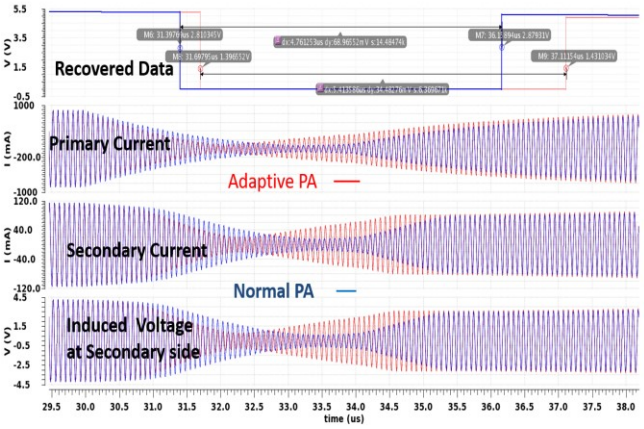

Fig. 5. Comparative analysis of received power for adaptive and normal PA

During the overall system simulation, we start the power modulation at 29.865 µs and stop the power modulation at 33.957 µs. There lies a trade-off between the bandwidth and power transferring capability of the system. The bit width of the downlink is increased by 1.6 µs (4.76µs to 6.36µs) for changing 'half-bridge PA resonance frequency' to 'full-bridge PA sub-harmonic frequency' power transmission protocol to frequency adaptive PA structure. However, the increment duration of the bit-width depends on the supply voltage and matching of the primary and secondary LC tank. During the transient phase, the power is increased by at least two times. The increment of bit width can be further reduced by an advanced ASK-based demodulator [7]. A detailed discussion of the local and global control structure or efficiency improvement of the whole system is beyond this paper's scope. It will be discussed in future publications. The primary focus of this paper is developing the digitally controlled adaptive PA structure.

VI. CONCLUSION

Through this brief, we analyzed downlink data modulation techniques using adaptive PA structure. This structure is helpful for transmitting a substantial amount of power during data transfer to prevent the abrupt shutdown operation in the implant due to the unavailability of power. Operating voltage and frequency are tuned simultaneously to have a better degree of freedom during power control. The data bit width is increased by 1.6 µs, whereas transmitted power is increased by approximately two times during the transient phase. The transmitter and receiver chips were designed in a 0.18-µm CMOS process using 1.8 V and 5V devices.

REFERENCES

[1] X. Li, Y. Li, C. Tsui, and W. Ki, "Wireless Power Transfer System With ΣΔ- Modulated Transmission Power Transmission Power and Fast Load Response for Implantable Medical Devices," in *IEEE Transactions on Circuits and Systems II: Express Briefs*, vol. 64, no. 3, pp. 279-283, March 2017

[2] Y. Park *et al.*, "A Frequency-Splitting-Based Wireless Power and Data Transfer IC for Neural Prostheses with Simultaneous 115mW Power and 2.5Mb/s Forward Data Delivery," *2021 IEEE International Solid-State Circuits Conference (ISSCC)*, 2021, pp. 472-474

[3] S. Sarkar and W. H. Ki, "Mathematical modeling of inductor current in class-D amplifier for wireless power transfer," *2020 IEEE Wirel. Power Transf. Conf. WPTC 2020*, vol. 1, no. 7, pp. 399–402, 2020.

[4] F. Bin Yang, J. Fuh, M. Takamiya, and P. H. Chen, "Structure-Reconfigurable Power Amplifier (SR-PA) and 0X/1X Regulating Rectifier for Adaptive Power Control in Wireless Power Transfer System," in *IEEE J. Solid-State Circuits*, pp. 1–11, 2020.

[5] C. Xia, R. Jia, Y. Wu, Q. Yu, and Y. Zhou, "WPIT technology based on the fundamental-harmonic component for a single-channel and two-coil ICPT system," in *IET Power Electron.*, vol. 12, no. 10, pp. 2608–2614, 2019.

[6] X. Li, Y. Lu, C. Tsui, and W. Ki, "An adaptive wireless powering and data telemetry system for optic nerve stimulation," *2014 IEEE International Symposium on Circuits and Systems (ISCAS)*, 2014, pp. 1404-1407.

[7] D. Ye, Y. Wang, Y. Xiang, L. Lyu, H. Min and C. -. R. Shi, "A Wireless Power and Data Transfer Receiver Achieving 75.4% Effective Power Conversion Efficiency and Supporting 0.1% Modulation Depth for ASK Demodulation," in *IEEE Journal of Solid-State Circuits*, vol. 55, no. 5, pp. 1386-1400, May 2020.

[8] B. Lee *et al.*, "An Implantable Peripheral Nerve Recording and Stimulation System for Experiments on Freely Moving Animal Subjects," in *Sci. Rep.*, vol. 8, no. 1, pp. 1–12, 2018.

[9] P. Schönle, F. Glaser, T. Burger, G. Rovere, L. Benini, and Q. Huang, "A Multi-Sensor and Parallel Processing SoC for Miniaturized Medical Instrumentation," in *IEEE J. Solid-State Circuits*, vol. 53, no. 7, pp. 2076–2087, 2018.

[10] S. Sarkar and W. -H. Ki, "Time Domain Analysis of Class-D Amplifier Driving Series-Series and Series-Parallel Circuits," *2020 IEEE REGION 10 CONFERENCE*, 2020, pp. 159-164.

[11] B. Lee and M. Ghovanloo, "An Overview of Data Telemetry in Inductively Powered Implantable Biomedical Devices," in *IEEE Communications Magazine*, vol. 57, no. 2, pp. 74-80, February 2019